

Design of Large Deflection Electrostatic Actuators

John D. Grade, Hal Jerman, and Thomas W. Kenny

Abstract— Electrostatic, comb-drive actuators have been designed for applications requiring displacements of up to 150 μm in less than 1 msec. A nonlinear model of the actuator relates the resonant frequency and the maximum stable deflection to the actuator dimensions. A suite of experiments that were carried out on DRIE, single-crystal silicon, comb-drive actuators confirm the validity of the model.

Four actuator design improvements were implemented. First, a folded-flexure suspension consisting of two folded beams rather than four and a U-shaped shuttle allowed the actuator area to be cut in half without degrading its performance. Second, the comb teeth were designed with linearly increasing lengths to reduce side instability by a factor of two. Third, the folded-flexure suspensions were fabricated in an initially bent configuration, improving the suspension stiffness ratio and reducing side instability by an additional factor of 30. Finally, additional actuation range was achieved using a launch and capture actuation scheme in which the actuator was allowed to swing backward after full forward deflection; the shuttle was captured and held using the backs of the comb banks as high-force, parallel-plate actuators.

Keywords— Comb Drive, Large Deflection Electrostatic Actuator, DRIE.

I. INTRODUCTION

MICROMACHINED devices for sensing of a wide variety of physical signals have been developed by hundreds of researchers, resulting in thousands of different devices [1]. Actuation methods in MEMS have been much harder to develop - especially when the application requires displacements of more than 50 μm . Some examples of actuators which have approached these displacements include thermal actuation approaches [2] [3], scratch drives [4] [5] [6], mechanically-amplified deflections [7] [8] [9], and the use of rotary motors and ratchets [10]. While all of these can achieve large displacements, the response time of these actuators is rarely less than 20 msec, and the amplification of the displacement usually comes at the cost of reduced force.

MEMS actuators which achieve fast response include miniaturized electromagnetic actuators [11] [12], and many different kinds of electrostatic actuators. Parallel plate actuators are used for many applications, including force rebalance in accelerometers [13] [14] [15], deformable optics [16], relays, and valves [17] [18]. Generally, these parallel-plate actuators have very limited range (usually 1/3 of the starting gap), and have to be feedback-controlled to achieve useful response.

J. D. Grade is with Iolon, Inc., San Jose, CA 95131. E-mail: jgrade@iolon.com .

H. Jerman is with Iolon, Inc., San Jose, CA 95131. E-mail: hjerman@iolon.com .

T. W. Kenny is with the Stanford Micro-Structures and Sensors Laboratory, Department of Mechanical Engineering, Stanford University, Stanford, CA 94305-4021. E-mail: kenny@cdr.stanford.edu .

More than 10 years ago, Tang and Howe introduced the comb-drive actuator for actuating polysilicon surface micromachined devices [19]. This device offered a nearly constant force over a large range of displacements, and became the preferred method for implementation of electrostatic actuation in many surface micromachined structures. The original Tang design is still widely used in its original form, and its availability through foundry processes has enabled very broad use.

This paper introduces substantial improvements to the original comb-drive design. Area-efficient designs are described that have a dramatically increased resistance to side instability. The result is a planar electrostatic actuator which offers more than 150 microns of displacement within 1 msec at an operating voltage of less than 150 V. The analysis of the electrostatic and mechanical side forces provides guidance for designers of comb drive actuators. The actuator redesign is carried out within the context of the recent developments in reactive ion etching [20] that enable aspect ratios of more than 20:1 in single-crystal silicon.

Side instability, sometimes called “side snap-over”, limits the static displacement of comb-drive actuators. The applied voltage and the overlapping comb area increase with forward displacement, leading to large cross-axis forces that cause the teeth to suddenly snap over sideways. As a result, large static deflections have only been reported for comb-drive actuators that were very large and quite slow [21]. This problem is widely known and has conventionally limited the displacement of comb drives.

Comb drives are attractive for the actuation of optical switches. A common design for a low port-count optical switch uses an actuator to insert a mirror into a collimated laser beam at a 45 degree angle, reflecting the light into a selected output port. A $1 \times N$ switch may be formed by using multiple actuators as shown in Figure 1 [29]. To move the mirror in and out of the optical path, the actuator must have a total deflection that is at least the width of the collimated beam. The divergence angle of the optical fiber and the focal distance of the lens determine the width of the collimated beam. Using 660 nm light with a typical fiber and lens, the beam remains collimated over a distance of 4 mm, and has 98% of its optical power within a 140 μm diameter. Therefore each actuator must travel a total distance of at least 140 μm , and the actuators for all of the output ports must fit along the 4 mm beam path.

This paper describes the design of area-efficient, comb-drive actuators with deflection ranges and actuation speeds that are suitable for optical switching applications. Also provided is a brief overview of the simple, robust fabrication process used to create the actuators. Finally, data is presented that confirms the electromechanical analysis,

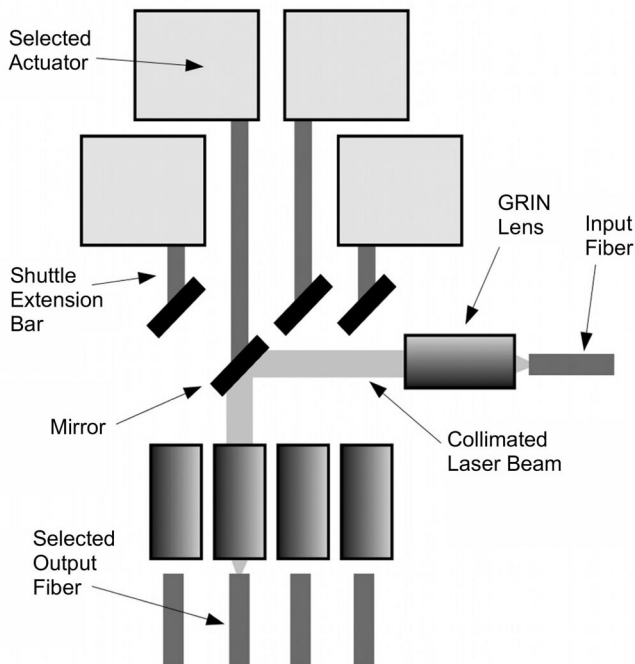


Fig. 1. Schematic diagram of a $1 \times N$ optical switch using multiple linear actuators. A laser beam, collimated by a GRIN lens, travels left until it is intercepted by an extended mirror and focused onto an output fiber.

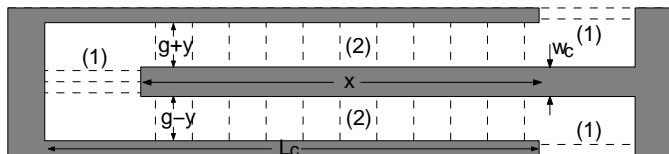


Fig. 2. Schematic drawing of a single comb pair showing the parallel-plate areas between (1) the tips and bases and (2) the overlapping sides of adjacent teeth.

shows stable deflections of as much as $180 \mu\text{m}$, and demonstrates optical switching performance.

II. ELECTROMECHANICAL ANALYSIS

Figure 3A shows the original comb-drive actuator with a folded-flexure suspension as described by Tang [22], [19]. This traditional actuator design is symmetric about both the x - and y -axes. The actuator design in Figure 3B is 50% smaller and is only symmetric about the y -axis. With half the combs and half the suspension beams of the traditional design, the motor deflection and fundamental resonant frequency remain substantially unchanged. Figure 3B also shows the folded suspension placed outside the combs to increase rotational stiffness. Figure 3C shows an actuator with two additional improvements: the combs vary in length, and the suspension is fabricated in an initially-bent configuration. These improvements delay the onset of electrostatic instability [28].

For any of the actuators in Figure 3, the actuator translates forward along the x -axis when a voltage is applied be-

tween the fixed and moving electrodes. As shown schematically in Figure 2, a relatively simple analytic approximation for the capacitance between the fixed and moving combs is given by the parallel-plate capacitances between the tips and bases and between the overlapped sides of adjacent teeth. For a single tooth this approximation is given by

$$C = \frac{2\epsilon h w_c}{L_c - x} + \frac{\epsilon h x}{g} \left(\left(1 - \frac{y}{g}\right)^{-1} + \left(1 + \frac{y}{g}\right)^{-1} \right), \quad (1)$$

where ϵ is the dielectric constant of air, h is the comb tooth height, x is the distance the combs are engaged, y is the comb displacement to the side, g is the gap between teeth, and w_c and L_c are the width and length of a comb tooth respectively. Equation 1 is only valid for positive deflections, but finite element analyses and experimental results indicate that when the comb teeth are engaged by at least 10%, Equation 1 is accurate to within 5%. The total capacitance is just the sum of the contributions from the individual teeth. The equation for the total capacitance may be refined to include the drop in capacitance when the comb teeth disengage as follows:

$$C = \frac{2N\epsilon h w_c}{L_c - x} + \frac{\epsilon A}{g} \left(\left(1 - \frac{y}{g}\right)^{-1} + \left(1 + \frac{y}{g}\right)^{-1} \right), \quad (2)$$

where N is the number of comb teeth and A represents the effective comb overlap area arising from a curve fit to a finite element analysis result for a pair of comb teeth. One fitting function for A is given by

$$A = \sum_{i=1}^N \left(h \int_{-\infty}^{x_i} \frac{1 + \tanh\left(\frac{x+b}{a}\right)}{2} dx \right), \quad (3)$$

where a and b are related to the slope and offset of the force transition that occurs when the teeth engage. For the actuators described in this work, reasonable values for a and b are $a = b = 7 \mu\text{m}$.

The electrostatic force is proportional to the voltage squared and the derivative of the capacitance, or

$$F_x = \frac{N\epsilon h w_c V^2}{(L_c - x)^2} + \frac{\epsilon A' V^2}{2g} \left(\left(1 - \frac{y}{g}\right)^{-1} + \left(1 + \frac{y}{g}\right)^{-1} \right), \quad (4)$$

where V is the voltage between the fixed and moving electrodes, and A' is the derivative of the fitting function, A , with respect to x . Figure 5 shows the electrostatic force as a function of the forward deflection calculated using Equations 1 and 2 to approximate the capacitance. In static equilibrium the forward electrostatic force is balanced by the restoring force of the suspension, $k_x x$, where k_x is the spring constant of the suspension in the forward direction.

Unfortunately, large electrostatic forces exist in the direction perpendicular to actuation. Using the capacitance given by Equation 2 with $x \ll L_c$, the side equilibrium

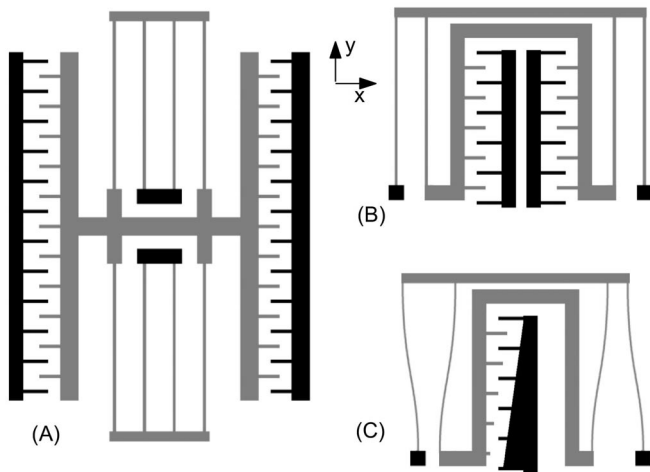


Fig. 3. Schematic drawing of (A) a traditional comb-drive actuator, (B) a comb-drive actuator with a U-shaped shuttle and only two folded-suspension beams, and (C) an improved comb-drive actuator with the suspension and comb teeth modified to achieve large deflections.

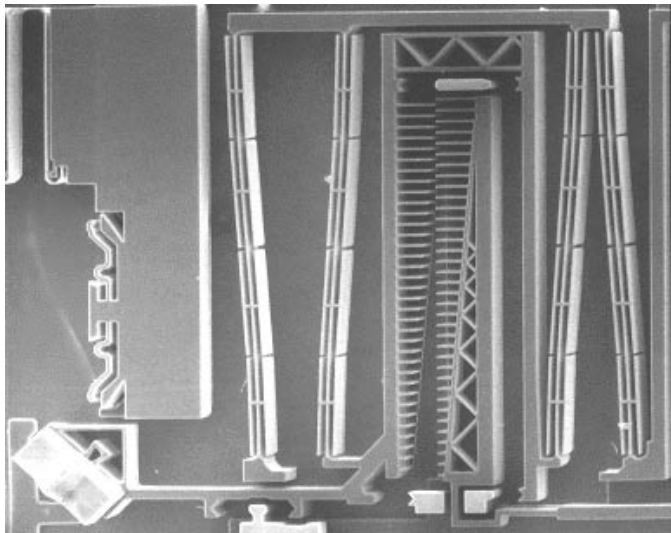


Fig. 4. Scanning electron microscope photograph of a comb-drive actuator with linearly engaging comb teeth and a prebent suspension.

equation is given by

$$k_y y = \frac{\epsilon A V^2}{2g^2} \left(\left(1 - \frac{y}{g}\right)^{-2} - \left(1 + \frac{y}{g}\right)^{-2} \right), \quad (5)$$

where k_y represents the stiffness of the suspension in the direction perpendicular to actuation. The stability of an equilibrium position depends on the curvature of the potential energy, which is equivalent to the derivative of the equilibrium equation. If an equilibrium position is unstable, then the potential energy is concave down:

$$k_y \leq \frac{\epsilon A V^2}{2g^3} \left(\left(1 - \frac{y}{g}\right)^{-3} + \left(1 + \frac{y}{g}\right)^{-3} \right). \quad (6)$$

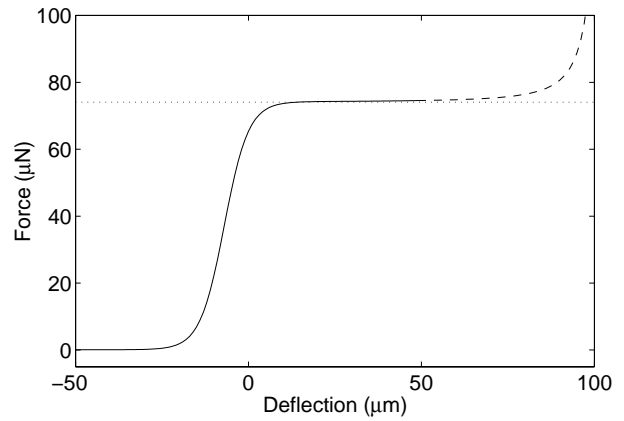


Fig. 5. Approximations to the electrostatic force with deflection. The dashed line corresponds to the first term in Equations 1 and 2, the dotted line corresponds to the second term in Equation 1, and the solid line corresponds to the second term in Equation 2.

Equation 6 may be simplified using Equation 4 to provide an equation for instability when $x \ll L_c$:

$$I = \frac{2k_x x}{k_y g^2} \frac{A'}{A} \frac{1 + 3(y/g)^2}{(1 - (y/g)^2)^2} \geq 1, \quad (7)$$

where we have defined the instability parameter, I , as the ratio of the sideways electrostatic forces to the sideways suspension forces. For standard comb drives with equal-length comb teeth, the equation for instability reduces to

$$I = \frac{2k_x x^2}{k_y g^2} \frac{1 + 3(y/g)^2}{(1 - (y/g)^2)^2} \geq 1, \quad (8)$$

In Equation 8, it cannot be assumed that $y = 0$. Non-ideal mechanical behavior, such as distortion of the shuttle during deflection, causes the actuator to follow a trajectory that contains a small sideways component, $e(x)$, *without* side electrostatic forces. The magnitude of $e(x)$ for the actuators considered in this work is about $0.5 \mu\text{m}$ over the forward deflection range. For actuators of the type shown in Figure 4, using $e(x) = 0.5(x/x_{max})$ and replacing $k_y y$ with $k_y(y - e(x))$ in Equation 5 results in side equilibrium positions, y , reaching 23% of the comb gap as x approaches x_{max} . This degree of comb misalignment increases side instability by 29%.

As discussed below, the form of the instability equation has been verified experimentally. In practice, actuators become unstable at deflections corresponding to a predicted value for I of about 65%. Thus, it is reasonable to design actuators that maintain $I < 20\%$ throughout their deflection range.

A. Linear Engagement Combs

While the parametric design of non-rectangular comb teeth that produce a nonlinear force as a function of deflection has been described [25],[26], the effects on side stability were neglected. An easy way to control the displacement

dependence of the force is to adjust the lengths of the individual rectangular comb teeth. A typical example is shown in Figure 4, where the lengths of the teeth of the moving electrode vary linearly. At full forward deflection the overlapping comb area is half that of a traditional comb drive. This reduction in overlap area causes the side electrostatic forces and side instability to be reduced by a factor of two as well. An additional benefit is the reduced actuator mass and increased resonant frequency.

Unlike the standard comb drive with equal-length combs, a linear-engagement comb drive has the forward force roughly proportional to the forward deflection. The number of engaged comb teeth varies linearly with forward displacement, and x_i in Equation 3 is given by

$$x_i = x - \frac{i-1}{N-1}x_{max}, \quad (9)$$

where the longest comb is x_{max} longer than the shortest comb. To illustrate the advantages provided by a linear-engagement comb drive, the forward electrostatic force in Equation 3 may be approximated by

$$F_x = \frac{N\epsilon h w_c V^2}{(L_c - x)^2} + \frac{N\epsilon h V^2}{2g} \left(\frac{x+b}{x_{max}} \right) \left(\left(1 - \frac{y}{g} \right)^{-1} + \left(1 + \frac{y}{g} \right)^{-1} \right), \quad (10)$$

where b is given by Equation 3. While the deflection is no longer proportional to the voltage squared, the voltage required to achieve x_{max} is the same as for the traditional case with equal-length combs. The equation for instability when $x \ll L_c$ is then given by

$$I = \frac{2k_x x^2 (x/2 + b)/x_{max}}{k_y g^2} \frac{1 + 3(y/g)^2}{(x+b)/x_{max} (1 - (y/g)^2)^2}, \quad (11)$$

and since $b \ll x_{max}$ the linear-engagement comb drive is twice as stable as the equal-length comb drive in Equation 8. Of course, the comb teeth need not vary linearly in length, and any additional reduction in the overlapping comb area would improve the side stability. However, changing the engagement profile, x_i , to further reduce the overlapping comb area would cause the actuator to require additional voltage to achieve full deflection [24].

B. Prebent Suspensions

With forward deflection in a comb-drive actuator, the undesired electrostatic side forces increase while the suspension's ability to resist them decreases. The electrostatic side forces may be reduced using linear-engagement combs. The stability may be further improved by customizing the suspension. The forward spring constant of the actuators shown in Figures 3B and 3C is given by

$$k_x = \frac{E h w_s^3}{L_s^3}, \quad (12)$$

where E is the bulk modulus of silicon (190 GPa), w_s is the suspension beam width, and L_s is the length of one

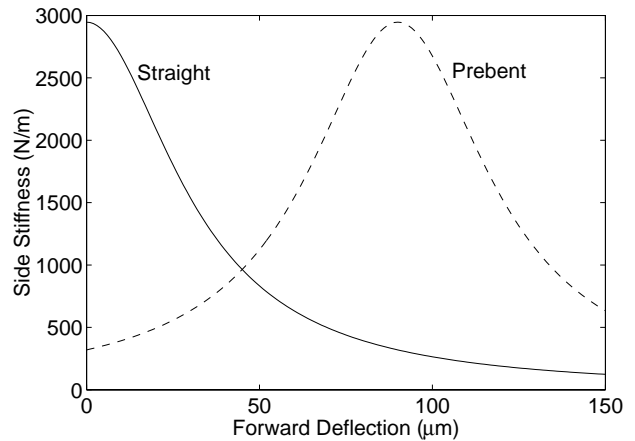


Fig. 6. Comparison of suspension side stiffness, k_y , versus forward deflection for suspensions that are $950 \mu\text{m}$ long and $4 \mu\text{m}$ wide with initially straight beams (solid) and prebent beams that straighten after $92 \mu\text{m}$ forward deflection (dashed). Typical stiffnesses of 5500 N/m and 7000 N/m are included in k_y for the shuttle and the bar linking the suspension beams.

of the four suspension beams. Equation 12 is accurate to within 0.1% for translations of up to 10% of the suspension beam length. The sideways suspension stiffness, however, is highly nonlinear. The side spring constant is actually a combination of the axial stiffness of the individual suspension beams and the geometric stiffness of the suspension as a whole [27] [24]. Ultimately, the side spring constant of the suspension is found to decrease with the square of the forward displacement:

$$k_y = \frac{8E h w_s^3}{3L_s x^2 + 8L_s w_s^2}, \quad (13)$$

where it has been assumed that the shuttle and the bar linking the folded suspension are infinitely stiff. Analytical and finite element models have indicated that neglecting the finite stiffness of the shuttle and bar typically overestimates the true side stiffness by 10% at full forward deflection [24]. Figure 6 shows the suspension stiffness in the side direction for the actuators shown in Figures 3B and 3C. Substitution of Equations 12 and 13 into Equation 11 gives

$$I = \frac{3x^4 + 8w_s^2 x^2}{8g^2 L_s^2} \frac{1 + 3(y/g)^2}{(1 - (y/g)^2)^2}. \quad (14)$$

Because side instability is proportional to x^4 , comb-drive actuators have typically been limited to applications requiring less than $40 \mu\text{m}$ of static deflection. The stable deflection range may be dramatically increased if the suspension beams are fabricated in an initially bent configuration such as in Figure 4. If the suspension beams straighten at a forward deflection x_{pb} , then $x - x_{pb}$ replaces x in Equation 13. The suspension stiffness in the side direction will then be low initially and increase as the suspension beams straighten with forward deflection. Thus the side stiffness is low when the side forces are low, and the side stiffness increases as the side forces increase. In the actuator shown

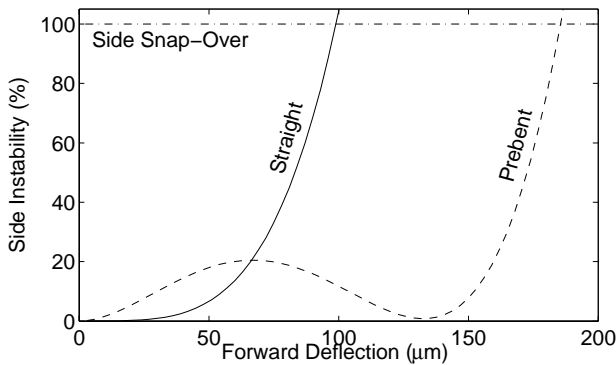


Fig. 7. Comparison of side instability, I , versus forward deflection for suspensions with initially straight beams (solid) and initially bent beams (dashed). Experimental results show the onset of instability at a calculated I value of about 65%. A robust design would have I less than 20%.

in Figure 4, the use of prebent suspension beams decreases the instability over the range of actuation by a factor of thirty. A graph comparing the stable operating ranges of straight and prebent suspensions is shown in Figure 7. In this example, the safe forward-deflection range ($I < 20\%$) has been increased by more than a factor of two simply by utilizing prebent beams.

III. DESIGN SPACE

Often, the design and dimensions of an actuator must be chosen to fulfill a given set of specifications. This section builds on the analysis of Section II to provide a method for the determination of the optimal actuator design in a particular application.

Ultimately, the available voltage is limited by dielectric breakdown between the electrodes. In many applications, however, the drive electronics provide a tighter constraint on the voltage available for actuation. The actuator must provide some specified deflection range, often while maintaining a minimum actuator speed or resonant frequency. In many cases, the maximum actuator size or cost is also specified. The stability of the actuator must be chosen based on the required device reliability, the anticipated operating environment, and the consistency of the fabrication process. If designs exist that satisfy the constraints, the actuator dimensions may then be chosen to optimize performance.

The basic parameters in comb-drive design are the dimensions of the suspension beams, the dimensions of the combs, the number of comb banks, the comb engagement profile, and the degree to which the suspension is initially bent. The switching application outlined in Section I requires that the side instability may not exceed 20% throughout the operational range. Also, the resonant frequency must be at least 750 Hz, using no more than 150 V.

The frequencies of the resonant modes may be calculated using finite element analysis [24], but the fundamen-

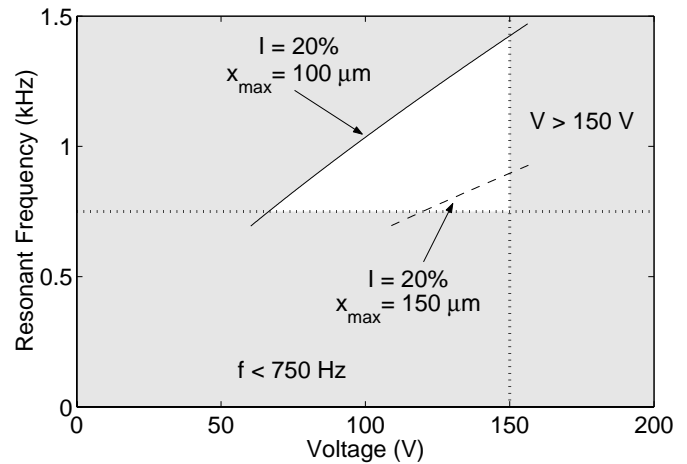


Fig. 8. Boundaries of the stability-voltage-frequency design space for an actuator with a prebent suspension and $100 \mu\text{m}$ of stable static deflection. The available design space is the clear central area in which $I < 20\%$, $V < 150 \text{ V}$, and $f > 750 \text{ Hz}$. The dashed line indicates the reduced design space for an actuator with a maximum stable deflection of $150 \mu\text{m}$.

tal mode is well approximated by

$$f_0 = \frac{1}{2\pi} \sqrt{\frac{k_x}{m}}, \quad (15)$$

where m is the mass of the moving portion of the actuator.

The width of the suspension beams and comb teeth is typically set to the minimum allowed by the fabrication process to minimize the actuator area. In the actuators described in this work, the minimum beam width is $4 \mu\text{m}$. Starting with the requirement that $I \leq 20\%$, Equation 14 defines the minimum comb gap, g , in terms of the suspension length. Equation 14 can then be used in Equation 4 to define the required voltage supply. Holding the actuator mass and number of comb teeth constant, the equations for the voltage and resonant frequency may be combined to form a single expression defining the stability of the voltage-frequency design space.

Figure 8 shows the resulting boundaries of the design space due to the voltage, resonant frequency, and stability constraints for an actuator with one bank of combs and a prebent suspension yielding $100 \mu\text{m}$ of forward deflection. An actuator with a straight suspension would be 30 times less stable, and the constraints on stability, resonant frequency, and voltage could not be simultaneously satisfied, regardless of the choice of suspension length.

As shown in Figure 8, the actuators could have a resonant frequency as high as 1.3 kHz or could have a drive voltage as low as 75 V, depending on the choice of suspension length. In Figure 8, the region corresponding to $I < 20\%$ is specific to a full deflection of $100 \mu\text{m}$. If a larger forward deflection range was required, the available design space would be reduced. The dashed line in Figure 8 shows the reduced design space that yields $150 \mu\text{m}$ of forward deflection. In fact, electrostatic actuators with stable deflections of $\pm 180 \mu\text{m}$ have been tested. These designs

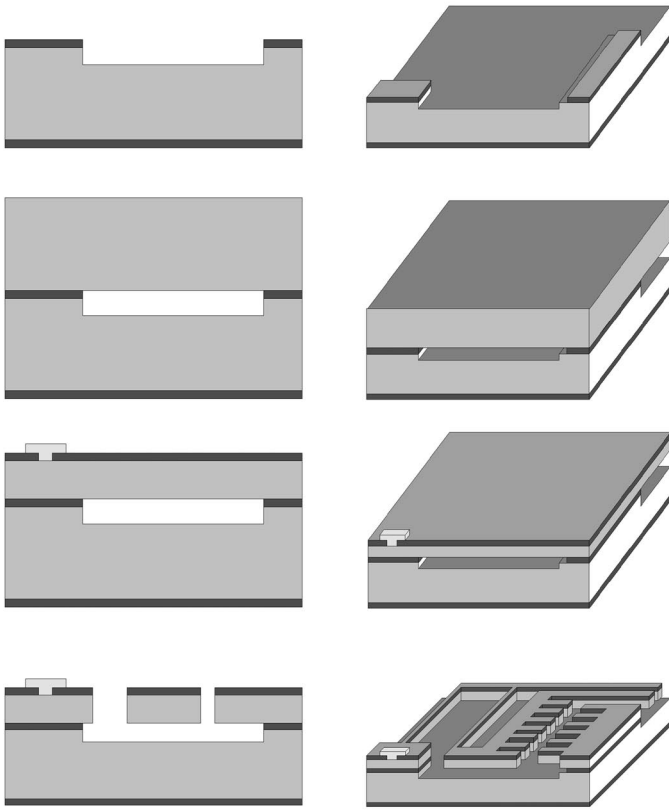


Fig. 9. Cross-sections and Isometric views of four steps in the fabrication process: (A) after the shallow cavity etch, (B) after fusion bonding, (C) after grind and polish and metal patterning, and (D) after the final DRIE step.

also used 150 V and had $f > 750$ Hz, but they were designed with a calculated maximum side instability of 50%.

IV. FABRICATION

Wafer fabrication was carried out at NovaSensor, in Fremont, California. While the proprietary details of the process were not disclosed, their fabrication process has been generally described [20]. A brief summary of the fabrication process is included here for reference.

The fabrication sequence is illustrated in Figure 9. As shown in Figure 9A, the process begins with a $390\ \mu\text{m}$ thick silicon wafer that will act as a carrier for the device wafer. The carrier wafer has a $1\ \mu\text{m}$ thick silicon dioxide layer and $10\ \mu\text{m}$ -deep etched areas that will provide a separation between the carrier and device wafers after wafer bonding. Those structures formed in the device wafer above the cavity will ultimately be free to move, while those structures formed outside the cavity etch will remain anchored to the carrier wafer.

The device wafer is fusion bonded to the front side of the carrier wafer (Figure 9B). The device wafer is then ground and polished to a bonded wafer pair thickness of $475\ \mu\text{m}$.

Aluminum is deposited on another thermally grown oxide layer which has etched holes for electrical contact to

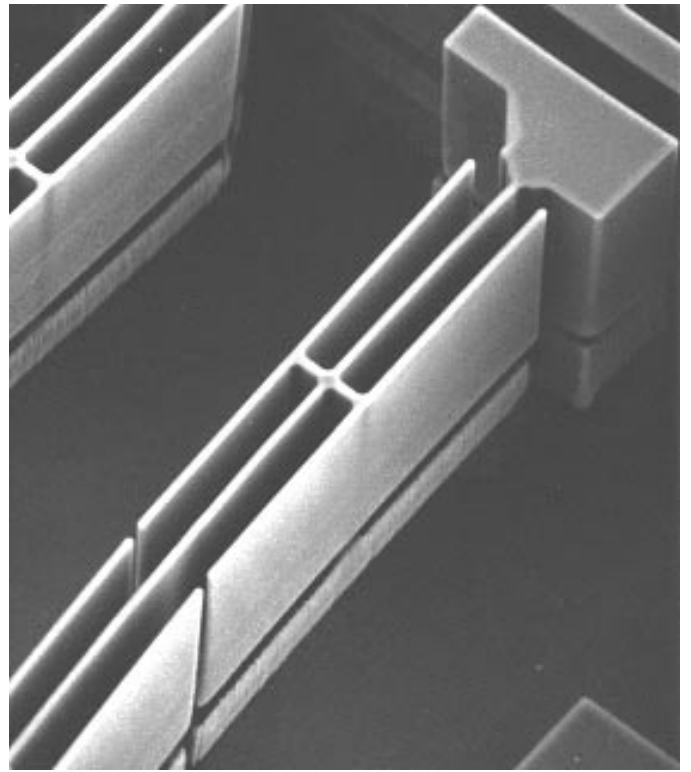


Fig. 10. Scanning electron micrograph showing an actuator suspension with a series of H-shaped etch fins to control the sidewall profile without affecting the suspension stiffness.

the silicon. The aluminum is then patterned to form pads for wire bonding (Figure 9C).

Finally, photoresist and the underlying oxide are used to define and protect the deep etched structures during a final deep reactive ion etch (Figure 9D).

As shown in Figure 4, the actuators in this work contain mirror holders, mechanical stops, and etch fins [28]. Separately fabricated mirrors are used with high-reflectivity optical coatings in order to achieve the highest optical efficiency and minimize scattering losses. The mirrors are attached and aligned to the motors using c-shaped mirror holders connected to arms extending from the shuttle [24]. The switching speed and positional accuracy are improved by using mechanical stops to define the fully retracted and fully extended actuator positions. Finally, a series of H-shaped fins are included along each suspension beam to control the sidewall profile and maintain etch uniformity during the DRIE step. As shown in Figure 10, the fins are not connected to each other, so they have little effect on motor performance. Addition of the fins typically increases the suspension stiffness by 1% and the moving mass by 8%.

V. EXPERIMENTAL RESULTS

The static behavior of actuators with both equal-length combs and linear-engagement combs was measured and compared to the model predictions. A separate set of actuators with equal-length combs was used to measure the dependence of stability and resonant frequency on the sus-

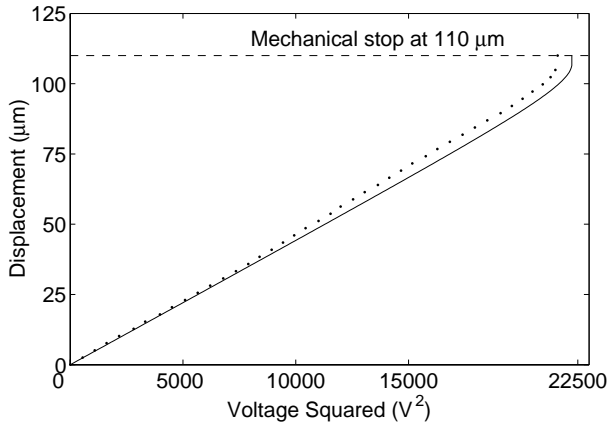


Fig. 11. Plot of the measured and predicted static deflection versus the voltage squared for an actuator with equal-length combs and mechanical stops at $110 \mu\text{m}$. The solid line corresponds to the analytical prediction using the nominal dimensions, and the circles correspond to the measured data points.

pension length and comb gap. Finally, the actuators were combined with mirrors, lenses, and fibers and assembled to form optical switches, allowing the switching speed to be measured.

A. Static Deflection

To capture the static behavior, the applied voltage was measured using a digital voltmeter with a resolution of 0.1 V , and the deflection was measured using a microscope at $1000\times$ magnification. The deflection measurements were repeatable to within $\pm 1 \mu\text{m}$. Figure 11 shows the deflection as a function of the voltage squared for actuators with equal-length combs and mechanical stops at $110 \mu\text{m}$. The maximum standard deviation over 5 samples was $2.3 \mu\text{m}$. The average resonant frequency was 849 Hz . The measured deflection was proportional to V^2 , with additional parallel-plate force from the comb tips appearing at about $100 \mu\text{m}$.

Figure 12 shows the forward displacement as a function of the voltage squared for an actuator with linearly-engaging combs and mechanical stops at $180 \mu\text{m}$. As expected, the measured deflection was a highly nonlinear function of V^2 . The solid line in the figure corresponds to the analytical prediction using the nominal dimensions. The discrepancy between the predicted and measured values corresponds to a $0.05 \mu\text{m}$ difference between nominal comb and suspension widths and the actual values. The resonant frequency of the actuator was 769 Hz . At maximum deflection, the predicted instability level for the actuator was 50% .

B. Side Instability

Two sets of actuators with equal-length combs and suspensions ranging from $600 \mu\text{m}$ to $1100 \mu\text{m}$ were used to measure side instability. The voltage was gradually increased until the comb drive became unstable, and the

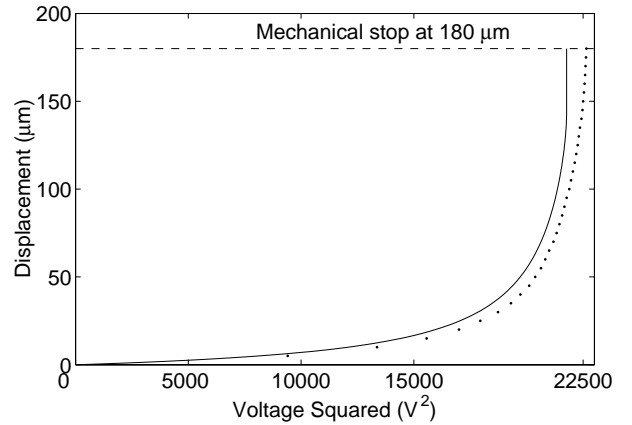


Fig. 12. Plot of the measured and predicted static deflection versus the voltage squared for an actuator with linearly-engaging combs and mechanical stops at $180 \mu\text{m}$. The solid line corresponds to the analytical prediction using the nominal dimensions, and the circles correspond to the measured data points. This actuator had a resonant frequency of 769 Hz .

TABLE I

MEASURED AND PREDICTED MAXIMUM STABLE DEFLECTION FOR MOTORS WITH $8.5 \mu\text{m}$ COMB GAPS AND SUSPENSION LENGTHS FROM $600 \mu\text{m}$ TO $1100 \mu\text{m}$.

Length	$I = 100\%$	$I = 50\%$	Measured Value
$600 \mu\text{m}$	$55.3 \mu\text{m}$	$43.7 \mu\text{m}$	$44.3 \mu\text{m}$
$700 \mu\text{m}$	$63.2 \mu\text{m}$	$50.8 \mu\text{m}$	$56.8 \mu\text{m}$
$800 \mu\text{m}$	$70.4 \mu\text{m}$	$57.2 \mu\text{m}$	$63.0 \mu\text{m}$
$900 \mu\text{m}$	$77.0 \mu\text{m}$	$63.0 \mu\text{m}$	$70.5 \mu\text{m}$
$1000 \mu\text{m}$	$83.2 \mu\text{m}$	$68.4 \mu\text{m}$	$75.3 \mu\text{m}$
$1100 \mu\text{m}$	$89.0 \mu\text{m}$	$73.5 \mu\text{m}$	$78.3 \mu\text{m}$

comb teeth snapped to the side. When the voltage was increased past about 80% of the snap-over value, the side deflection of the comb teeth became visible. Just prior to side instability, the comb teeth were off-center by about 25% of the comb gap, as predicted by the models described above.

Ten measurements of the maximum stable deflection and the corresponding drive voltage were made on each actuator. For each of the actuators, the snap-over voltage measurements were repeatable to within $\pm 2\%$. The snap-over deflections for the actuators with $8.5 \mu\text{m}$ gap combs are shown in Table I, and the deflections for the actuators with $6.5 \mu\text{m}$ gap combs are shown in Table II, along with the predicted values for $I = 50\%$ and $I = 100\%$.

C. Resonant Frequency

A Polytec OFV 501 fiber interferometer was used to quantify the resonant behavior of the actuators with suspension lengths from $600 \mu\text{m}$ to $1100 \mu\text{m}$. Based on the analysis in Section II-B, the resonant frequency should be proportional to the suspension length to the $3/2$ power. As shown in Table III, the data and the predicted values

TABLE II

MEASURED AND PREDICTED MAXIMUM STABLE DEFLECTION FOR MOTORS WITH 6.5 MICROMETER COMB GAPS AND SUSPENSION LENGTHS FROM 600 MICROMETERS TO 1100 MICROMETERS.

Length	$I = 100\%$	$I = 50\%$	Measured Value
600 μm	44.8 μm	34.8 μm	35.2 μm
700 μm	52.0 μm	41.1 μm	45.5 μm
800 μm	58.5 μm	46.9 μm	51.2 μm
900 μm	64.4 μm	52.2 μm	56.0 μm
1000 μm	69.9 μm	57.1 μm	59.8 μm
1100 μm	75.0 μm	61.6 μm	64.4 μm

match to within 3%. The quality factor of the fundamental resonance was about 60 for the actuators described in this work.

TABLE III

MEASURED AND PREDICTED RESONANT FREQUENCIES FOR MOTORS WITH SUSPENSION LENGTHS FROM 600 MICROMETERS TO 1100 MICROMETERS.

Length	Predicted Value	Measured Value
600 μm	2163 Hz	2190 Hz
700 μm	1714 Hz	1670 Hz
800 μm	1385 Hz	1360 Hz
900 μm	1161 Hz	1120 Hz
1000 μm	985 Hz	980 Hz
1100 μm	833 Hz	820 Hz

D. Switching

As described in Section II-B, instability in comb drive actuators is proportional to x^4 . The most common method of increasing the deflection range is to operate the actuator in both directions around the rest position in a “push-pull” configuration. This requires a larger actuator with combs in both directions, but it cuts the required deflection in a single direction in half, providing a 16 \times improvement in stability. In switching applications where continuous analog positioning is not required, a different strategy may be employed. In a “launch and capture” configuration, the actuator still operates in both directions around the rest position, but parallel plate electrodes replace the combs in one of the directions. Applying voltage to the combs retracts the shuttle against a set of mechanical stops. Removing the voltage allows the shuttle to swing freely toward another set of stops in the extended direction. The free deflection of the shuttle depends on the quality factor, Q . The maximum free deflection in the extended direction is $(1 - 2/Q)$ less than the starting deflection in the retracted direction. When the shuttle nears the stops, the voltage is applied to the parallel plates. As shown in Figure 3, the back side of the comb bank may be used to form the parallel plate electrode. Thus the state of the actuator is toggled by removing the drive voltage, waiting between $1/2f$ and $1/4f$,

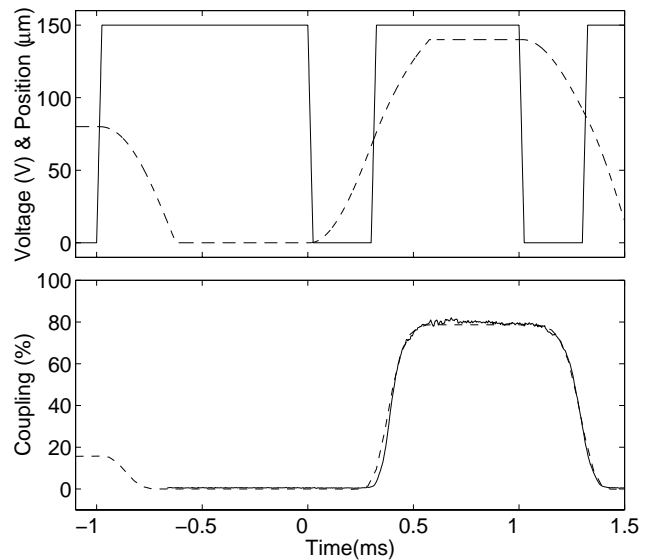


Fig. 13. Measurements and predicted values during dynamic switching. Top graph: measured drive voltage (solid) and calculated motor position (dashed). Bottom graph: measured (solid) and calculated (dashed) optical coupling efficiency.

and reapplying the voltage.

Since dynamic switching only requires combs in the retracted direction, the actuator footprint may be smaller than that of an actuator designed for static switching. The potential drawback to the dynamic switching strategy is the timing required to reliably transition from one state to the other. An example actuator that employs the launch and capture actuation strategy is shown in Figure 4. Metalized silicon mirrors were attached to actuators of this type for use in an optical switch with a 140 μm wide laser beam, shown schematically in Figure 1. The coupling efficiency was measured using Newport 1830C optical power meters at the input and output fibers during switching.

The top graph of Figure 13 shows the motor position, calculated by a simple second-order SimulinkTM system model, along with the measured drive voltage during dynamic switching. The bottom graph shows the measured optical coupling and the coupling predicted by the interception the gaussian laser beam by the mirror. This actuator operated using slightly less than 150 V. Note that the voltage applied to the combs is also present on the parallel plate clamps. The off-on switching time was 0.5 msec from the command to 95% of maximum optical power. The on-off switching time was 0.4 msec from the command to 5% of maximum optical power.

Since dynamic switching requires a timed voltage pulse, it is important to characterize the dependence of switching errors on the applied voltage and pulse length. Figure 14 shows a contour plot of the average number of errors per 1000 switching trials as a function of the applied voltage and pulse length for three sample actuators. The large white region in the center of the contour plot represents the area with no errors. The four outer regions correspond to error rates of up to 10, 100, 200, and 500 per 1000 trials.

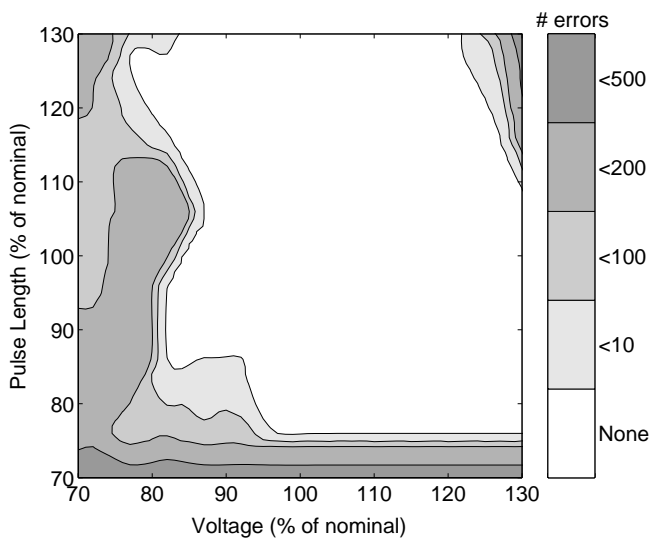


Fig. 14. Sensitivity of dynamic switching to voltage and pulse length. The large white region in the center of the contour plot represents switching with no errors in 1000 trials.

The applied voltage and pulse length in Figure 14 are represented as a percentage of their respective nominal values.

The data in Figure 14 indicate that reliable switching may be achieved for variations in applied voltage and pulse length of more than $\pm 10\%$. Similarly, for a given switching waveform, the actuator's required voltage and resonant frequency may vary by the same amount while still maintaining switching reliability. The relative insensitivity to voltage and resonant frequency variations make dynamic driving a viable actuation strategy for applications that do not require continuous position control.

VI. CONCLUSIONS

The development of large-range, high-speed electrostatic actuators has been possible since the emergence of DRIE etching of planar flexures. However, this development required the optimization of several aspects of comb-drive actuators. This paper described methods for increasing the cross-axis stiffness of the flexures, allowing position control at both extreme locations of the actuator, and reducing the overall footprint of the system. An optimized actuator is described which allows 150 micron range of deflection within 1 ms and with operating voltages below 150 V. Experimental results presented in this paper demonstrate that this device operates with performance that matches model predictions, and that volume production can be carried out with high yield and high device uniformity. These concepts and optimization strategies are generally applicable to comb-drive actuator design, and should be of use throughout the community of designers that have adapted comb-drives to a wide variety of applications.

ACKNOWLEDGMENTS

The authors would like to thank Kathy Jackson and Howard Lee at Iolon, and Sam Wong at Novasensor for

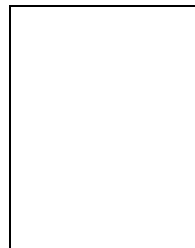
their help with fabrication, assembly, and testing.

REFERENCES

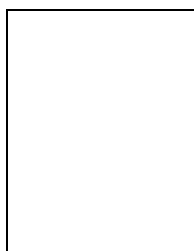
- [1] E. Thielicke and E. Obermeier, "Microactuators and their technologies," *Mechatronics*, vol. 10, no. 4-5, pp. 431-455, June-August 2000.
- [2] D.E. Sene, V.M. Bright, J.H. Comtois, and J.W. Grantham, "Polysilicon micromechanical gratings for optical modulation," *Sensors and Actuators A-PHYSICAL*, vol. 57, no. 2, pp. 145-151, November 1996.
- [3] J.H. Comtois and V.M. Bright, "Applications for surface-micromachined polysilicon thermal actuators and arrays," *Sensors and Actuators A-PHYSICAL*, vol. 58, no. 1, pp. 19-25, January 1997.
- [4] T. Akiyama and K. Shono, "Controlled stepwise motion in polysilicon microstructures," *Journal of Microelectromechanical Systems*, vol. 2, no. 3, pp. 106-110, September 1993.
- [5] T. Akiyama, D. Collard, and H. Fujita, "Scratch drive actuator with mechanical links for self-assembly of three-dimensional MEMS," *Journal of Microelectromechanical Systems*, vol. 6, no. 1, pp. 10-17, March 1997.
- [6] M.C. Wu, "Micromachining for optical and optoelectronic systems," in *Proceedings of the IEEE*, November 1997, vol. 85, No. 11, pp. 1833-1856.
- [7] R.A. Brennen, M.G. Lim, A.P. Pisano, and A.T. Chou, "Large displacement linear actuator," in *Proceedings of Solid-State Sensor and Actuator Workshop*, Hilton Head Island, South Carolina, June 1990, pp. 135-139.
- [8] S. Kota, J. Hetrick, Z. Li, and L. Saggere, "Tailoring unconventional actuators using compliant transmissions: design methods and applications," in *IEEE/ASME Transactions on Mechatronics*, Hilton Head Island, South Carolina, December 1999, vol. 4, pp. 396-408.
- [9] M.S. Rodgers, S. Kota, J. Hetrick, Li Zhe, and B.D. Jensen, "A new class of high force, low-voltage, compliant actuation systems," in *Proceedings of Solid-State Sensor and Actuator Workshop*, Hilton Head Island, South Carolina, June 2000, pp. 210-213.
- [10] J.J. Sniegowski, S.L. Miller, G.F. LaVigne, M.S. Rodgers, and P.J. McWhorter, "Monolithic geared-mechanisms driven by a polysilicon surface-micromachined on-chip electrostatic micro-engine," in *Proceedings of Solid-State Sensor and Actuator Workshop*, Hilton Head Island, South Carolina, June 1996, pp. 178-182.
- [11] W.P. Taylor, O. Brand, and M.G. Allen, "Fully integrated magnetically actuated micromachined relays," *Journal of Microelectromechanical Systems*, vol. 7, no. 2, pp. 181-191, June 1998.
- [12] W.P. Taylor, M. Schneider, H. Baltes, and M.G. Allen, "Electroplated soft magnetic materials for microsensors and microactuators," in *Proceedings of the International Conference on Solid-State Sensors and Actuators*, Chicago, USA, June 1997, vol. 2, pp. 1445-1448.
- [13] ADXL05 accelerometer, Analog Devices, Norwood, MA.
- [14] C. Yeh and K. Najafi, "CMOS interface circuitry for a low-voltage micromachined tunneling accelerometer," *Journal of Microelectromechanical Systems*, vol. 7, no. 1, pp. 6-15, 1998.
- [15] C.H. Liu and T.W. Kenny et al., "Characterization of a high-sensitivity micromachined tunneling accelerometer with micro-g resolution," *Journal of Microelectromechanical Systems*, vol. 7, no. 2, pp. 235-244, 1998.
- [16] G. Vdovin, P.M. Sarro, and S. Middelhoek, "Technology and applications of micromachined adaptive mirrors," *Journal of Micromechanics and Microengineering*, vol. 9, no. 2, pp. R8-R19, June 1999.
- [17] P.M. Zavracky, N.E. McGruer, R.H. Morrison, and D. Potter, "Microswitches and microrelays with a view toward microwave applications," *International Journal of RF and Microwave Computer-Aided Engineering*, vol. 9, no. 4, pp. 338-347, July 1999.
- [18] L. Yobas, M.A. Huff, F.J. Lisy, and D.M. Durand, "A novel bulk-micromachined electrostatic microvalve with a curved-compliant structure applicable for a pneumatic tactile display," *Journal of Microelectromechanical Systems*, vol. 10, no. 2, pp. 187-196, June 2001.
- [19] W. Tang, T. Nguyen, and R. Howe, "Laterally driven polysilicon resonant microstructures," *Sensors and Actuators*, vol. 20, pp. 25-32, 1989.

- [20] E. Klaassen, K. Petersen, J. Noworolski, J. Logan, N. Maluf, J. Brown, C. Storment, W. McCulley, and G. Kovacs, "Silicon fusion bonding and deep reactive ion etching; a new technology for microstructures," *Sensors and Actuators*, vol. 52, pp. 132–139, 1996.
- [21] W. Hofman, C. Lee, and N. MacDonald, "Monolithic three-dimensional single-crystal silicon microelectromechanical systems," *Sensors and Materials*, vol. 10, pp. 337–50, 1998.
- [22] W. Tang, *Electrostatic comb drive for resonant sensor and actuator applications*, Ph.D. thesis, Department of Electrical Engineering and Computer Sciences, University of California, Berkeley, California, November 1990.
- [23] M. Judy, *Micromechanisms Using Sidewall Beams*, Ph.D. thesis, Department of Electrical Engineering and Computer Sciences, University of California, Berkeley, California, April 1994.
- [24] J. Grade, *Large-deflection high-speed electrostatic actuators for optical switching applications*, Ph.D. thesis, Department of Mechanical Engineering, Stanford University, Stanford, California, January 2000.
- [25] J. Mohr, M. Kohl, and W. Menz, "Micro optical switching by electrostatic linear actuators with large displacements," in *Proceedings of the 7th International Conference on Solid-State Sensors and Actuators*, Yokohama, Japan, June 1993, pp. 120–123.
- [26] W. Ye, S. Mukherjee, and N. MacDonald, "Optimal shape design of an electrostatic comb drive in microelectromechanical systems," *Journal of Microelectromechanical Systems*, vol. 7, no. 1, pp. 16–26, March 1998.
- [27] R. Legtenberg, A. Groeneveld, and M. Elwenspoek, "Comb-drive actuators for large displacements," *Journal of Micromechanics and Microengineering*, vol. 6, pp. 320–329, 1996.
- [28] J. H. Jerman, J. D. Grade, J. D. Drake, *Electrostatic microactuator and method for use thereof*, U.S. Patent 5,998,906, 1999.
- [29] J. H. Jerman, J. D. Grade, J. D. Drake, K. E. Petersen, *Optical data storage system having optical microswitch*, U.S. Patent 6,134,207, 2000.

patents in the field of micromachining with more than 20 additional US patent applications pending.

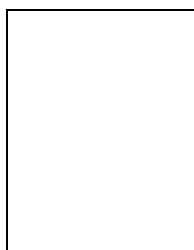


Thomas W. Kenny received the B.S. degree in physics from the University of Minnesota, Minneapolis, in 1983 and the M.S. and Ph.D. degrees in physics from the University of California, Berkeley, in 1987 and 1989, respectively. He worked at the Jet Propulsion Laboratory, Pasadena, CA, where his research focused on the development of electron-tunneling-based high-resolution microsensors. Since 1994, he has been Assistant Professor and Terman Fellow with the Mechanical Engineering Department, Stanford University, Stanford, CA. He currently oversees graduate students in the Stanford Microstructures and Sensors Laboratory, whose research activities cover a variety of areas such as mechanical measurements on biological structures including molecules, gecko hairs, and insects, development of integrated wafer-scale encapsulation of MEMS devices, and ultrasensitive force sensors for MRFM. He recently took leave from Stanford to co-found Cooligy, a venture-funded startup developing novel liquid cooling technologies for microprocessors.



John D. Grade is Manager of Micromachining Design at Iolon, Inc. He is responsible for the modeling and design of micromachined actuators, components, sub-mounts, and tooling. He was a micromachining design engineer at Seagate Research in San Jose, California, building upon his work at Quinta Corporation in large-displacement actuation and precision tooling. He also worked at IC Sensors on high-performance micromachined sensors for gas detection. John currently holds ten US patents

with several others pending. His academic background is in mechanical engineering, having earned his B.S. working in robotics at the California Institute of Technology and his M.S. and Ph.D. working on micromachined sensors at Stanford University.



Hal Jerman is Senior Director of Micromachining Development and Founder of Iolon, Inc. He received his B.S. degree in Applied Physics and M.S. degree in Electrical Engineering from the California Institute of Technology and his Ph. D. degree from Stanford University in 1981 for work on integrating a gas chromatograph on a silicon wafer. He was a founder of Microsensor Technology (now part of Agilent) and worked at IC Sensors (now part of Silicon Microstructures), Quinta Corp., and Seagate

prior to his current position. His earlier work was involved with a wide variety of physical sensors and actuators, including thermal conductivity detectors, bimetallic gas valves, medical infusion restrictors, inertial-grade accelerometers, automotive intake air flow sensors, miniature PCR reactors, capillary electrophoresis devices, and optical data storage heads. His current work involves the design and development of high aspect ratio electrostatic actuators for use in optical modules for telecommunications systems. He holds 40 issued US